Influence of synthesis parameters on the short-range structure and electrochemical performances of Li2MnO2F

Quentin Deville, Romain Wernert, Valérie Dillay, Benoît Mortemard de Boisse, Marie Guignard, Dany Carlier

Influence of synthesis parameters on the short range structure and electrochemical performances of Li_2MnO_2F

Quentin Deville[1], Romain Wernert[1,2,4], Valérie Dillay[4], Benoît Mortemard de Boisse[4],

Marie Guignard[1,2], Dany Carlier*[1,2,3]*

AUTHOR ADDRESS

[1] Université de Bordeaux, CNRS, Bordeaux INP, ICMCB, UMR 5026, F-33600 Pessac, France

[2] RS2E, Réseau Français sur le Stockage Electrochimique de l'Energie, FR CNRS #3459, Amiens F-80039 Cedex 1, France

[3] ALISTORE-ERI European Research Institute, CNRS 3104, 80039 Amiens Cedex 1, France

[4] SAFT, 111-113 Boulevard Alfred Daney, 33074 Bordeaux, France

KEYWORDS: Li-ion batteries, positive electrode material, disordered rocksalt, oxyfluoride, MAS-NMR, oxygen redox

Corresponding authors email address:

dany.carlier@icmcb.cnrs.fr

marie.guignard@icmcb.cnrs.fr

ABSTRACT:

In the last years, disordered rocksalt structure materials (DRS) was proposed as positive electrode for lithium-ion batteries. In particular, the fluorinated DRS were proposed to be more stable upon cycling than pure oxides counterparts. These materials are mainly obtained by mechanosynthesis in order to incorporate a significant amount of F ions and maintain a disordered structure. Since the local structural arrangement is crucial for battery application, we aim to monitor its evolution upon the synthesis of Li_2MnO_2F from two sets of precursors: Mn_2O_3, Li_2O and LiF, or $LiMnO_2$ and LiF. The synthesis progress was thus followed, by ^{7}Li and ^{19}F MAS-NMR coupled to XRD to probe the structure at different scale. This allowed to identify an optimal milling time to reach the final compounds. We show that they exhibit similar morphology (by SEM), medium- and short-range orders (by XRD, ^{7}Li and ^{19}F NMR, EXAFS) and average Mn oxidation degree (by XANES). The electrochemical performances of the two compounds are almost similar, with high specific capacities of 319 $mAh.g^{-1}$ ("from $LiMnO_2$") and 304 $mAh.g^{-1}$ ("from Mn_2O_3") for the first charge to 4.8 V vs Li^{+}/Li, proving their interest as post-NMC candidates as positive electrode materials.

Introduction:

The last years have seen the development of fluorinated lithium-rich (Li-rich) disordered rocksalt structure materials (DRS) used as positive electrode materials in lithium batteries[1]. In contrast to layered oxides, where Li^+ ions are intercalated in the interslab space, in Li-rich DRS materials, the transition metal (TM) and Li ions share the same octahedral sites in the lattice. Lithium diffusion is thus three-dimensional and relies on percolation pathways which are only observed for a Li excess Li/M~1.3 and Li/M disorder[2–4] DRS materials are expected to be more stable upon cycling than Li-rich layered oxides thanks to their three-dimensional structure. High capacities for those materials, larger than those based on the redox activity of the transition metal ion, are observed due to contribution of the oxygen to the redox process, which however induces significant capacity loss. Fluorine substitution of O has been proposed as an efficient way to limit the capacity loss[3,5,6] and, as the same time, to increase the capacity based on the TM ions, thanks to the increase of their oxidation state. For example, compared to $Li_2Mn^{IV}O_3$ (model compound for Li-rich layered oxides), partial O substitution by F, leads to $Li_2Mn^{III}O_2F$ where the Mn^{3+}/Mn^{4+} redox couple can be active. This fluorination therefore prevents the use of heavy elements such as Nb or Mo for substitution to Mn to do so[5].

DRS materials had proven being able to deliver reversible capacities over 300 $mAh.g^{-1}$ with various active redox metals : Li_2VO_2F[6], $Li_2V_{0.8}Cr_{0.2}O_2F$[7], Li_2FeO_2F[7], $Li_{1.25}Mn_{0.5}Nb_{0.25}O_2$[8], $Li_{1.2}Mn_{0.4}Ti_{0.4}O_2$[9] or $Li_4Mn_2O_5$[10] as well as $Li_{1+x}MoO_2F_x$ [11] and $Li_{1.25}TiO_2F_{0.25}$[7] . In this kind of materials, local order has been shown to strongly influence electrochemical performances[12–14].

Li_2MnO_2F is an interesting and challenging positive electrode material that has recently been studied by the groups of P. Bruce and S. Islam.[5,15,16]. In a first paper, House et al. [5] focused on Li_2MnO_2F obtained by ball milling from a Mn_2O_3 precursor. They report the structural study of the material carried out by X-Ray Diffraction (XRD) and solid-state ^7Li and ^{19}F Nuclear Magnetic

Resonance (NMR) as well as the electrochemical performances of the material (291 $mAh.g^{-1}$ at C/10 rate with a retention of 160 $mAh.g^{-1}$ after the 50^{th} cycle). Moreover, they highlighted an oxygen loss that can be associated with an oxygen-redox mechanism if more than one Li/mole is deintercalated. It was further confirmed by the work of Sharpe *et al*.[15] which proved the presence of trapped molecular O_2 within the lattice as well as O_2 gas release from the surfaces. In a very recent work on this material based on ab initio molecular dynamics (AIMD), McColl *et al.*[16] confirmed that O_2 molecules are formed in the bulk during the lithium electrochemical deintercalation. They showed that Mn migration to interstitial sites (five- or sixfold coordinated sites) and the appearance of cation vacancies were necessary to form O_2 in the bulk. During the discharge of the cell, some of the O_2 molecules would be reduced to O^{2-} and return to their atomic position in the face-centered cubic lattice, while others would remain trapped in the bulk as $O_2(g)$ due to irreversible migration [16].

Since the role of the disorder in those materials is crucial for their electrochemical properties, we aimed in the present study to investigate the impact of the synthesis conditions of Li_2MnO_2F by ball milling on both the local structure and the electrochemical properties. Mechanosynthesis was chosen because as it has been demonstrated to produce materials with high disorder as well as large integration of fluorine in the bulk.[3,5,17] In this study, we monitor the progress of the synthesis depending on the milling time and precursors type: Mn_2O_3, Li_2O and LiF, or $LiMnO_2$ and LiF. We especially focus on the medium- and short-range orders by using XRD and solid state NMR. Finally, we compare the morphology (SEM), the medium- and short-range orders (XRD, NMR, EXAFS), average oxidation degree (XANES) and the electrochemical performances of the two final Li_2MnO_2F compounds.

Experimental:

Mechanosynthesis was performed using a planetary ball miller (Fritsch, Pulverisette 7 Premium line), which allowed using airtight ball milling jars under argon atmosphere. For the synthesis of Li_2MnO_2F, two different routes were used:

$2LiF + Li_2O + Mn_2O_3 \rightarrow 2Li_2MnO_2F$ Pathway denoted "from Mn_2O_3"

$LiMnO_2 + LiF \rightarrow Li_2MnO_2F$ Pathway denoted "from $LiMnO_2$"

$LiMnO_2$ in its orthorhombic form was obtained through the synthesis proposed by Croguennec *et al.*[18], LiF (99.85%, AlfaAesar), Mn_2O_3 (99%, SigmaAldrich), Li_2O (98%, Sigma Aldrich) were otherwise commercial. The precursors were first dried before entering in glove box and then homogenized by manual grinding using an agate mortar and pestle.

The target weight of Li_2MnO_2F was 5g and the precursors were used in the stoichiometric proportions, 50 g of 2mm zirconium oxide beads (ball to powder ratio 10:1) were added to the jar. These conditions were determined by preliminary experiments detailed in the Supporting Information (**Fig S1**). Both bowls and beads were made of zirconium dioxide with a Vickers hardness of 1200 (Vickers Pyramid Number). A 36-hour ball milling was conducted over the two studied pathways. To prevent an important increase of the temperature in the bowl (reagents, products, beads and bowls), the milling sequence alternated 10 min of milling at 750 rpm with a 10 min break. 0.5 g of the powder were sampled and unclogged from bowl walls at the following milling times: 6 h, 12 h, 18 h and 36 h for the final products. The bowl walls are also unclogged after milling for 9 h. 5 g of beads were also removed from the bowls to maintain the ball-to-powder ratio. The clogged powder was recovered as much as possible using a sieve, but it is important to note that due to the bead size, removing the powder on each bead is not achievable. Therefore, the mass of the removed beads included a fraction of powder which was considered as lost for the

experiment. Once the mechanochemical synthesis was achieved, the product was stored in a glovebox, as it is highly air sensitive.

Characterizations:

NMR:

The ^{7}Li and ^{19}F Magic Angle Spinning (MAS) NMR spectra were recorded on a Bruker Avance III 100 MHz spectrometer (2.35T). A standard Bruker 2.5 mm MAS probe at a 30 kHz typical spinning speed was used. The samples were loaded in the rotors in a glovebox. The spectra were recorded using one period rotor-synchronized Hahn echo sequences with 90° pulse of 2 µs. Prior to our analysis, we verified that our experimental conditions lead to a good quantification regarding the recycling delay and the use of the Hahn echo sequence: the recycling delay (D1) was optimized through testing different time duration between 0.5 s and 900 s for materials prepared with different milling times. The optimized conditions are reported in the **Table 1:** for $t_{milling}$ = 0 h, longer D1 were necessary to avoid T_1 saturation, since some ^{7}Li and ^{19}F nuclei are expected to be located in diamagnetic environments, which have the longest T1 relaxation time compared to paramagnetic environments. On the contrary, for $t_{milling} \geq 6$ h, shorter recycle delays as short as 0.5 s were long enough to avoid T_1 saturation effects. This already indicated a rather close proximity of the ^{7}Li and ^{19}F nuclei to the paramagnetic Mn ions centers in those materials (**Fig S2, Table S1**). This showed that all ^{19}F signals have similar T2 relaxation times, so the Hahn echo sequence used here provide a correct relative quantification of the signals. The external references used is a 1M LiCl aqueous solution for ^{7}Li and $CFCl_3$ for ^{19}F spectra. Li_2MnO_2F spectra have been normalized with respect to the sample masses and scan number.

Table 1. Optimized NMR acquisition parameters for ^{7}Li and ^{19}F-NMR spectra

		$t_{milling}$ = 0h	$t_{milling}$ ≥6h
^{7}Li	D1 (s)	300	0.5
	Scan number	208	20480
^{19}F	D1 (s)	120	0.5
	Scan number	512	20480

Powder X-ray diffraction (XRD): A Panalytical Empyrean diffractometer with an X'Celerator detector and operating with a Cu K_{α} source and an Bruker airtight poly(methyl methacrylate) dome coupled with a silicon sample holder were used to follow the milling progression by XRD. The radiations were generated at 45 kV and 40 mA ($\lambda(K_{\alpha1})$ = 1.5406 Å and $\lambda(K_{\alpha2})$ = 1.5444 Å). The sample holder was filled in a glovebox (Ar). Profile refinements using the Le Bail method were performed with Jana2006 software[19].

Lattice representations : Figures were drawn with Vesta[20].

Electrochemistry:

Self-supported electrodes were prepared using a 65/25/10 weight w_t.% ratio of active material (AM) / Carbon black / PTFE binder. 10 mm diameter electrodes were cut and pressed on a 16 mm diameter aluminum grid, which was used to improve the electrical conductivity within the cathode. 2032 coin cells were assembled using 2 sheets of Celgard 2500 as separators and a total of 120 µL of electrolyte spread evenly on the surface of the cathode and each separator layer. The electrolyte

is property of Saft company and performs adequately over the studied range of 2.0 – 4.8 V vs Li^+/Li with known limitations at high potential. The positive electrodes were tested vs a 16 mm diameter, 300 µm thick Li metal disk and the coin cells were sealed with a manual cell crimper from Hohsen.

The coin cells were cycled on either a Perkin-Elmer VMP or BioLogic MPG-2, and were tested with two techniques: cyclic voltammetry or galvanostatic cycling. The voltage window for cyclic voltammetry was set between 2.0 and 4.8 V at a scan rate of 0.1 mV/s, corresponding to a forward sweep of almost 8 hours. Galvanostatic cycling was set in the same voltage range and for cycling rates C/10 and C/20, where C is calculated from the theoretical specific capacity (440 mAh/g), considering that 2 Li^+ ions per Li_2MnO_2F formula unit can be extracted. Capacity retention was calculated from the first discharge capacity. The voltage limits for long term cycling tests were chosen to avoid the possible reduction of manganese to the Mn(II) state during the reduction process and to trigger O-redox at high voltage.

X-ray absorption spectroscopy (XAS):

XAS was performed at the XAFS beamline, Elettra Sincrotrone, Trieste (Italy), which was operating with a storage ring energy of 2.4 GeV and a typical current of 160 mA (top-up mode) at the time of the measurements. The white beam was monochromatized with a pair of Si(111) crystals. Samples were diluted in cellulose and pelletized with a mass loading calculated so that the edge jump at Mn K edge is equal to 0.8. The pellets were packed in Ar-filled plastic bag to avoid air exposure and measured in transmission geometry. A Mn metal foil was used for the energy calibration of all samples by setting the first inflection point to 6539 eV. $LiMnO_2$ and Li_2MnO_3 were used as reference samples for the edge position of Mn(III) and Mn(IV). $LiMnO_2$ synthesis was described above and Li_2MnO_3 was synthesized by solid state reaction of Li_2CO_3 and

$MnCO_3$ heated for 5 h at 500°C and then for 10 h at 900°C. ATHENA from the Demeter software suite was used to process the spectra[21].

Scanning electron microscopy (SEM) :

A JEOL JSM-6700 F electron microscope with a theoretical resolution of 1.1 nm has been used. Samples were metallized with CCU-010 compact coating unit with a tungsten target at 40 mA. A 10 nm layer coating resulted from this operation. The voltage of the field emission gun was set at 5.0 kV and the working distance was set at 25 mm for low magnification (MAG), 5-6mm for the other MAG and 15 mm for EDS mapping.

Results and discussion:

Average and local structures:

The progress of the mechanosynthesis was studied by *ex situ* XRD by collecting 500 mg in the milling bowl after each milling steps. In **Figure 1,** the evolution of the XRD patterns shows the disappearance of precursor-associated peaks as the milling time increased and the appearance of the 002, 022 and 222 peaks of the rocksalt structure described using a Fm-3m space group. 36 hours were necessary to obtain a full disappearance of all precursor-associated peaks for both Li_2MnO_2F obtained "from Mn_2O_3" and "from $LiMnO_2$". In order to compare the two final products, Le Bail profile refinements of their XRD patterns were performed as presented in **Figure 2**. The lattice parameter of the two final Li_2MnO_2F phases was 4.12(2) Å "from Mn_2O_3" and 4.15(2) Å "from $LiMnO_2$", which are consistent with the calculated value of 4.13 Å for a cubic cell from Shannon's table of ionic radii considering a random distribution of Li^+ and Mn^{3+} ions in the octahedral sites of the face-centered cubic structure[22]. However, these values should be considered with caution in view of the peak width and the few reflections recorded in our conditions. Indeed, mid-height widths were respectively of 2.53° and 2.55° (2θ) for the 45° peak for Li_2MnO_2F "from Mn_2O_3" and "from $LiMnO_2$", corresponding to coherent domain sizes as

small as 3 to 5 nm according to Scherrer's law. From this XRD study, it can be concluded that both pathways lead to very similar Li_2MnO_2F products at a long range scale.

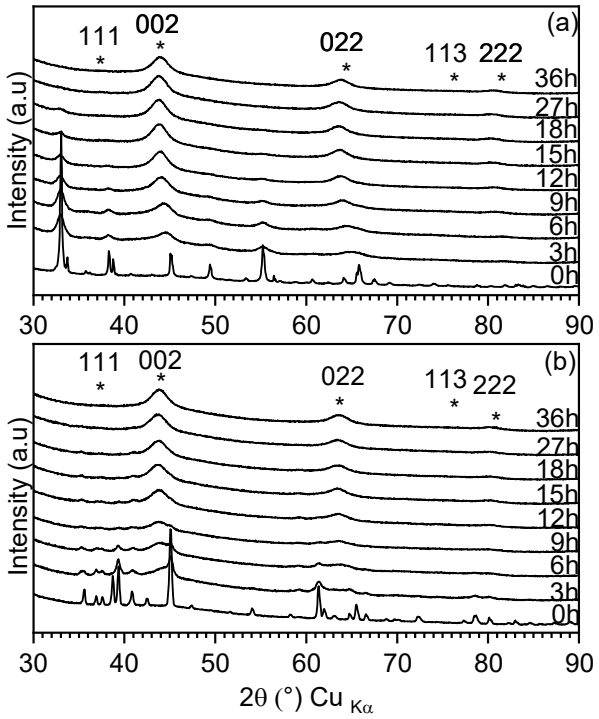

Figure 1. *Evolution of XRD patterns through the mechanosynthesis progress depending on the precursors setting: "from Mn_2O_3" (top) and "from $LiMnO_2$" (bottom).*

The intensities of the XRD peaks are rather similar for the two samples, but since F^- and O^{2-} have the same electronic configuration and hence similar X-ray scattering factors, the anion distribution in the lattice cannot be investigated by this technique. Moreover, the Li ions are barely detectable by XRD. Consequently, ^7Li and ^{19}F MAS-NMR spectra were recorded to probe the evolution of the local environment of these elements during the mechanosynthesis process. Due to the large broadening of the signals expected from the hyperfine interaction between unpaired electrons of Mn^{3+} ions and ^{19}F or ^7Li nuclei, a low external magnetic field (2.35T) was used for all MAS-NMR acquisitions. Such technique has already been used in other studies for the local characterization of DRS materials, which indeed showed large signals.[23–25]

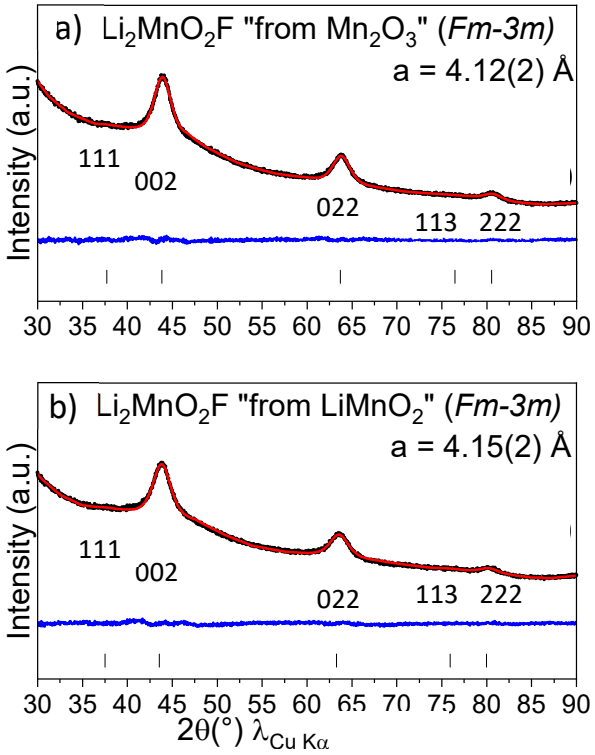

Figure 2. *Experimental XRD patterns and Le Bail profile refinement of Li_2MnO_2F samples after 36 h of milling (a) " from Mn_2O_3", a = 4.12(2) Å, R_p = 0.92, R_{wp} = 1.14 (b)" from $LiMnO_2$", a = 4.15(2) Å, R_p = 1.07, R_{wp} = 1.36. For both, in black the experimental patterns, in red the fit and in blue the difference.*

Figure 3 shows the zoomed ^{19}F MAS-NMR spectra of the samples at different milling times (0, 6, 12, 18, 36 h) for both pathways. At t = 0 h (spectrum also visible in full scale in **Figure 4)**, *i.e.* after the manual grinding of the precursor mixture, one can observe mainly the ^{19}F signal at -204 ppm assigned to F nuclei in the LiF diamagnetic phase and a small additional broad contribution around -110 ppm assigned to F nuclei interacting with some paramagnetic Mn^{3+} ions ($3d^4$: t_{2g}^3, e_g^1 electronic configuration).

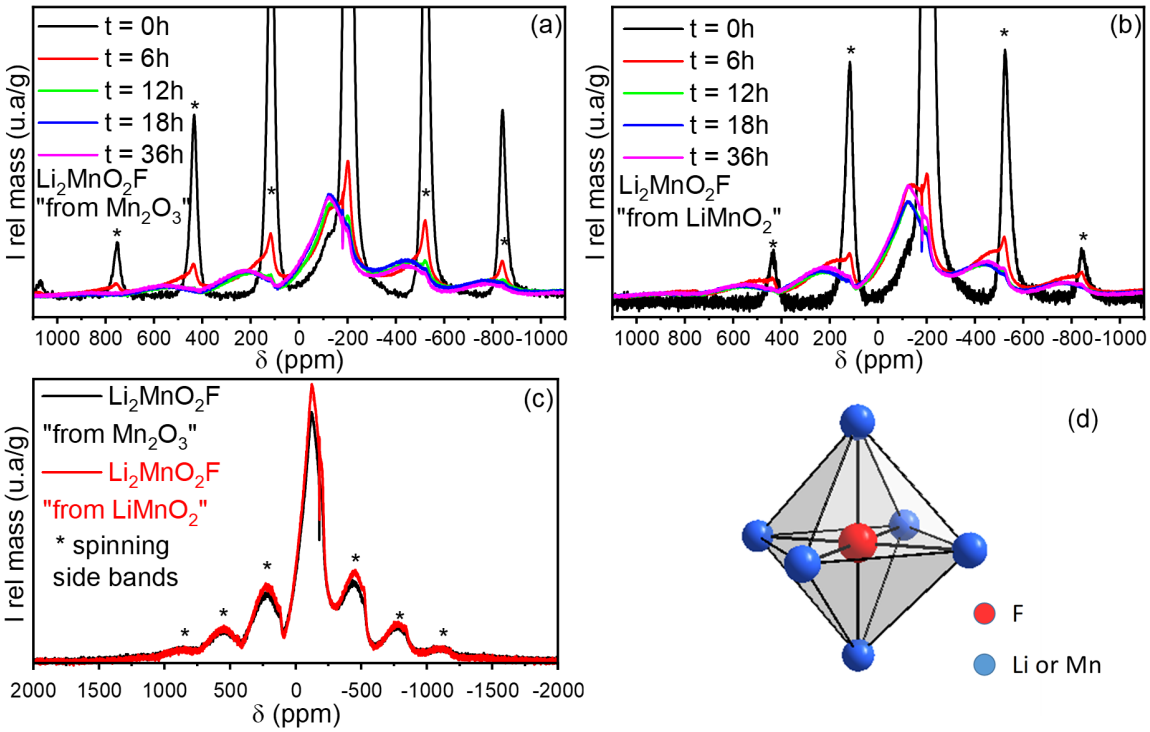

Figure 3. *^{19}F MAS NMR spectra of the samples obtained through the mechanosynthesis process as a function of the precursors a) "from Mn_2O_3" b) "from $LiMnO_2$", c) a comparison of the two final Li_2MnO_2F compounds and d) representation of the F local octahedral environment: $F(Li,Mn)_6$.*

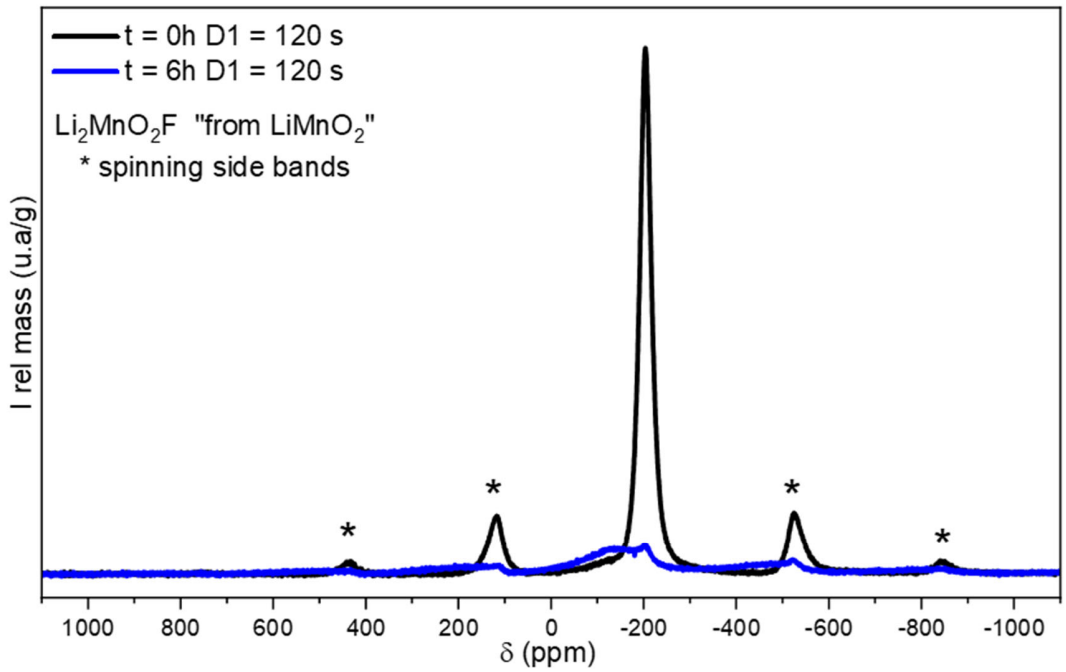

***Figure 4**: [19]F MAS-NMR spectra of the samples before milling (t = 0 h) and after 6 h of milling, on the pathway Li_2MnO_2F "from $LiMnO_2$" measured with two D1*

Therefore, the manual mixing has already initiated the reaction. Moreover, the signal assigned to LiF exhibits much broader spinning side bands manifold than pure LiF (**Figure S3**), due to nucleus spin-electron spin dipolar interaction, occurring through space, which indicates a close proximity between LiF and the paramagnetic precursor after the manual mixing. As the ball milling time increases, the intensity the LiF signal decreases as that of the broad contribution increases. From the local F environment (**Figure 3d**), a strong positive Fermi contact shift of ^{19}F is expected from the hybridization between Mn e_g and F 2s orbitals as they form σ-type overlap, whereas a weaker negative shift is expected from the hybridization of the Mn t_{2g} and F 2p orbitals (π overlap), which would negatively polarized deeper levels involving the F 2s orbital.[26,27] As a result, a positive Fermi contact shift, *i.e.* higher ppm values compared to LiF, is observed experimentally. However, it has been suggested in the literature that F adjacent to a Mn^{3+} cannot be observed due to too large

hyperfine interaction.[28] We have therefore compared here the intensity of the "t=0 h" and "t=6 h" spectra recorded under the same conditions (with a long D1 = 120s delay). It appears that around 52.3% of the fluorine nuclei are not observable in the "t=6 h" sample compared to "t=0 h". In case of a statistical distribution of Li and F in the sample, if all F ions adjacent to at least one Mn^{3+} ion were not observed *i.e.* F – Mn_x ($1 \leq x \leq 6$), one would expect a loss of 91.2% in intensity (**Supporting Information-S4**). Thus, the intensity measured in the "t=6 h" sample, which is also representative of the intensities obtained for samples prepared with longer milling times, is 5 times higher than this theoretical prediction. It implies F – Mn_x (probably with low x values) environments are well detected by ^{19}F MAS NMR, despite the paramagnetic feature of manganese. Ab initio calculations would be required to fully understand the distribution of the shifts across the different possible F environments, but are beyond the scope of this study. Therefore, we aimed here mainly to model the overall paramagnetic contribution, *i.e.* F surrounded by at least one Mn^{3+} ion as first neighbor, versus the "diamagnetic one", *i.e.* F surrounded only by Li^+ ions (LiF-like), to follow the synthesis. Due to significantly different line shapes of the "diamagnetic" F-Li_6 environment and the F-$Li_{6-k}Mn_k$ environments with $k \geq 1$, a small error would be obtained for the ratio between the "diamagnetic" and "paramagnetic" contributions. The methodology used for the spectra decomposition is reported in the Supporting Information (**Fig S5**). **Figure 5** shows the evolution of the ratio between the "diamagnetic" and "paramagnetic" contributions as a function of the milling time. It reaches a plateau around 18 h of milling for the two synthesis routes indicating no further evolution of the product. This ratio corresponds to the expected value considering a statistical Li/Mn distribution around F (8.8% of the fluorine nuclei are surrounded only by lithium ions), which tends to indicate that the samples are well disordered (Supporting Information-S4).

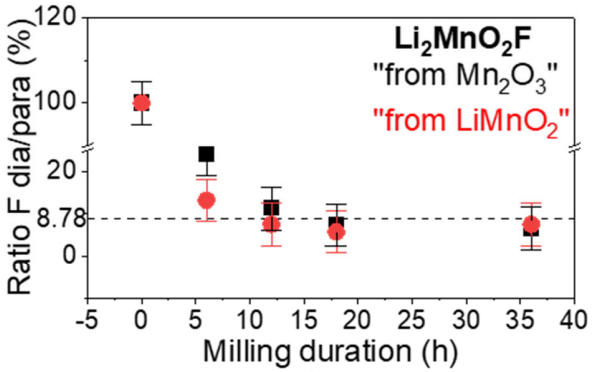

Figure 5. *Evolution of the ^{19}F intensity ratio of F in diamagnetic environment (narrow signal at -204 ppm) versus F in paramagnetic one (broad signal) through the synthesis sampling for both pathways.*

The progress of the syntheses by the two different pathways was also monitored by ^{7}Li MAS-NMR as shown in **Figure 6**. For t = 0h, the spectra of the two sets of precursors are, as expected, different: two signals are observed for $LiF+LiMnO_2$, one around 0 ppm for LiF and one at +36 ppm for $LiMnO_2$, since it contains paramagnetic Mn(III) in the vicinity of lithium. As for the ^{19}F NMR, the intensity of the narrow Li signals in a diamagnetic environment (~0 ppm) decreases with increasing milling time, while the broad Li signal of Li in paramagnetic environments increases in the 0-600 ppm range. The spectral decomposition is complex as many different Li environments exist. Indeed, through Fermi contact interactions, the electron spins of Mn can delocalize through two main spin transfer pathways, depending on the local geometry (**Figure 6d**) : when Mn^{3+} ions are Li 1^{st} neighbors, the interaction occurs at 90° either directly or through O or F, and when the Mn^{3+} ions are Li 2^{nd} neighbors, the interaction occurs at 180° through O or F. Since each Li site has 12 first cationic neighbors (90° interaction) and 6 second neighbors (180° interaction), many signals can overlap, 91 to be exact. The resolution of the spectra was not sufficient to distinguish the different contributions, which overlap strongly here.

As with for ^{19}F MAS-NMR, we wanted to compare the evolution of Li intensities in "paramagnetic" versus "diamagnetic" environments as a function of the milling time and synthesis pathway (**Figure 7** and decomposition in **Figure S6**). As for ^{19}F NMR, no more evolution of the ratio is observed after 18h of milling time. The theoretical probability of having only Li ions located as first and second neighbors around a given Li when Li/Mn are statistically distributed is equal to 0.068%. However, the experimental value reached here is much higher, around 6%, suggesting preferential distribution around Li. Since the ^{19}F ratio reached was close to that expected one for a statistical repartition of Li and Mn, this observation tends to show that the extra diamagnetic Li environments are more likely to be oxygen-rich.

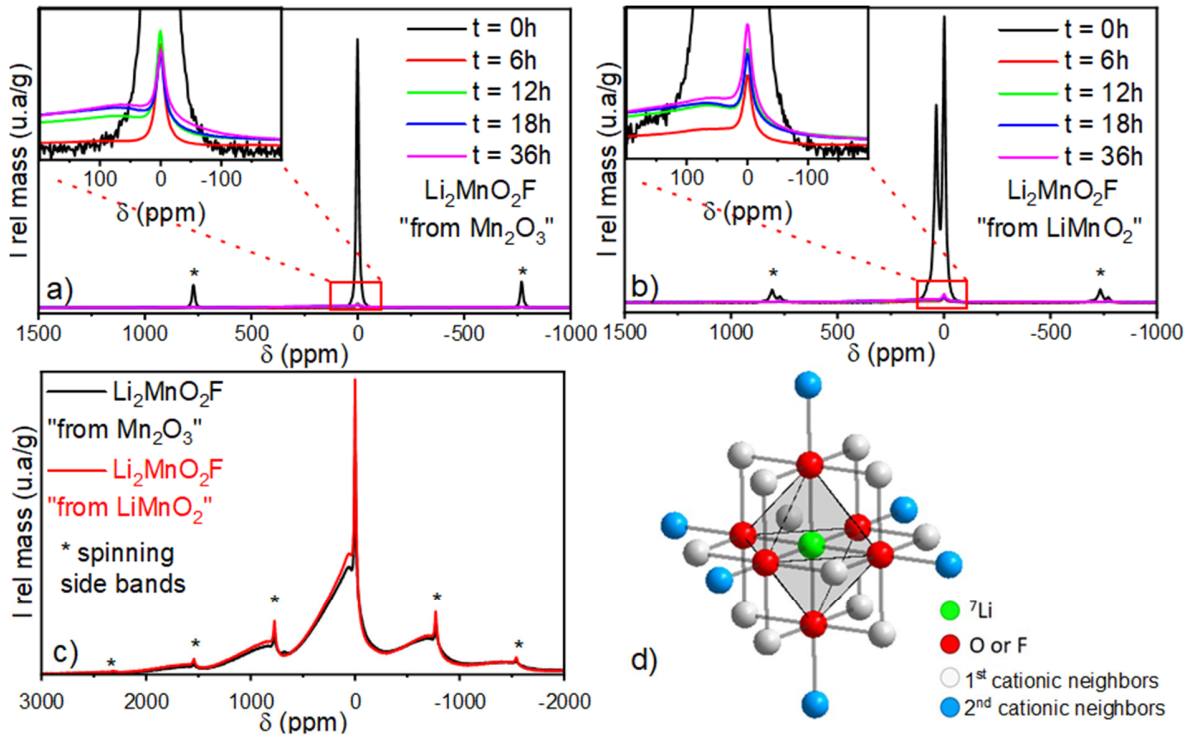

Figure 6. *^{7}Li MAS-NMR spectra of the samples through the mechanosynthesis process as a function of the precursors a) "from Mn_2O_3", b) "from $LiMnO_2$", c) a comparison of Li_2MnO_2F obtained from both after 36 h and d) Representation of the cationic sites surrounding ^{7}Li.*

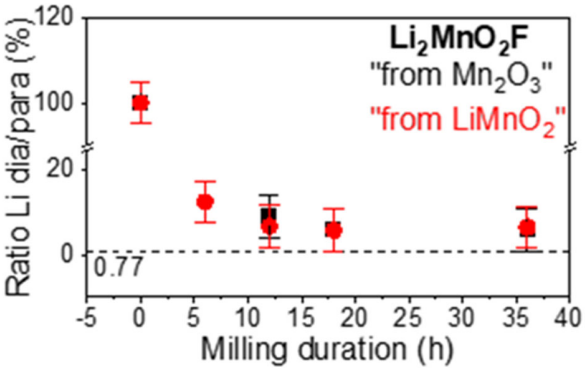

Figure 7. *Evolution of the ^{7}Li intensity ratio of Li in diamagnetic environment (narrow signal at 0 ppm) versus Li in paramagnetic one (broad signal) through the synthesis sampling for both pathways.*

From the NMR study we can conclude that the ^{19}F and ^{7}Li NMR spectra of the two final products are very similar showing a similar local arrangement close to the statistical one, highlighting that the choice of precursors has little or no influence on the final product structure. The syntheses were replicated and observed by each technique. The ^{19}F spectra of the replicates are provided **Figure S7**.

The Mn local structure and its oxidation state in both Li_2MnO_2F samples were also probed by Mn K-edge XAS. The near edge region of Li_2MnO_2F, where the main edge features the dipole that allows 1s → 4p transitions, is shown in **Figure 8** together with $LiMn^{III}O_2$ and $Li_2Mn^{IV}O_3$ used as reference compounds. The position and shape of the edges and pre-edges of both disordered rocksalts were well overlaid with the Mn(III) reference, confirming the expected oxidation state very close to +III. Although the shape of the edge of the two Li_2MnO_2F samples was identical, a small energy shift of 0.37 eV (at a normalized absorption of 1) could be observed for the sample "from Mn_2O_3" compared to the "from $LiMnO_2$" sample. Since the two Mn(III) and Mn(IV) references showed a shift of 2.40 eV for an absorption equal to 1, the sample "from Mn_2O_3" was

expected to be slightly over-oxidized by ~0.15 e^- as compared to the other one. Careful *a posteriori* XRD investigation of the precursors revealed traces of MnO_2 (1.6%) in the commercial Mn_2O_3 precursor (**Figure S8**), which was assumed to be the cause of the deviation from pure Mn(III) in the product.

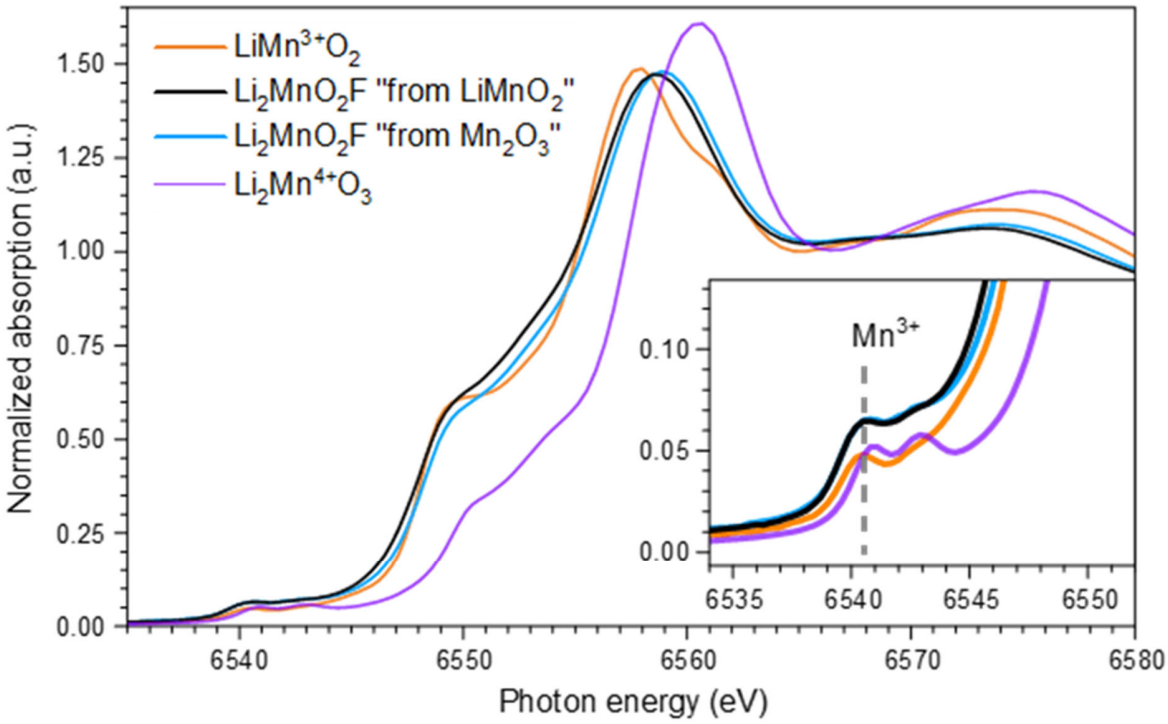

Figure 8. *X-ray absorption spectra of Li_2MnO_2F samples synthetized from $LiMnO_2$ or Mn_2O_3. $LiMnO_2$ and Li_2MnO_3 are used as Mn(III) and Mn(IV) references, respectively.*

EXAFS fits were performed with 2 shells around Mn (**Figure 9**). The first shell represented Mn-O bonds which were divided into 2 sets of distances due to the Jahn-Teller effect (2 M-O bonds of the same distance and 4 M-O of a different distance) (**Table 2**). Indeed, considering a single set of 6 equivalent Mn-O distances did not fit the data well. The second shell corresponded to Mn-Mn bonds. Similar results (within the precision of the fit) were obtained for both materials, again demonstrating the equivalence of the two synthesis pathways. Thus, our results tend to show that there is a local distortion of the MnO_6 octahedron in Li_2MnO_2F, contrary to the model proposed

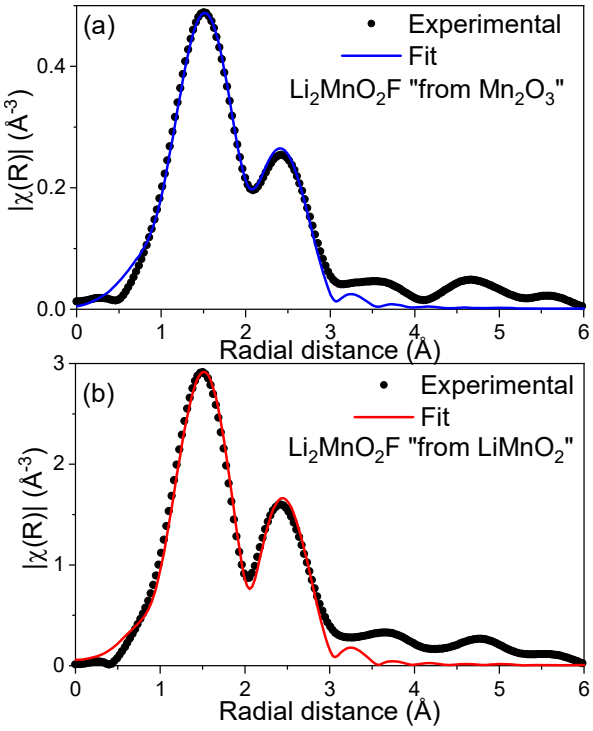

Figure 9. *EXAFS fit performed on Li_2MnO_2F samples synthetized (a) "from Mn_2O_3" or (b)" from $LiMnO_2$".*

by Sharpe *et al.*[15] These results indicate that the local structure is in fact quite different from that expected from the average rock salt structure, and that the distortion of the coordination sphere around the manganese ions inevitably distorts that of the lithium ions as well. However, the link between the Li polyhedral local distortion and the Mn one is not trivial, since many different Li environments versus Mn^{3+} ions are expected, so each polyhedron might exhibit a different distortion.

Table 2. *EXAFS fitted parameters obtained for Li_2MnO_2F "from Mn_2O_3" (in black) and "from $LiMnO_2$" (in red).*

Material Li_2MnO_2F	Bond	N (total fixed to 4)	R(Å)	Debye-Waller factor (10^{-3} Å^2)
"from Mn_2O_3" / "from $LiMnO_2$"	Mn-O	4 / 4	1.90(2)/1.91(3)	9.33/9.96
	Mn-O	2 / 2	2.24(3)/2.23(0)	9.33/9.96
	Mn-Mn	2.69(8) / 2.67(0)	2.90(5)/2.91(4)	17.22/18.30

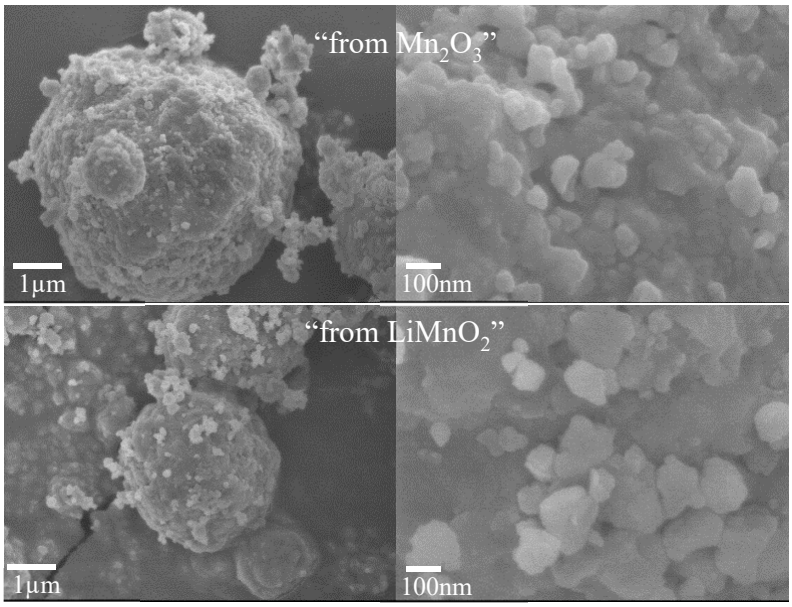

Figure 10. *SEM images of the Li_2MnO_2F samples obtained "from Mn_2O_3" (top row) and "from $LiMnO_2$" (bottom row).*

The SEM images displayed in **Figure 10** show similar morphologies and particle sizes for the samples obtained by both pathways. Over the two pathways, it seems that Li_2MnO_2F obtained "from $LiMnO_2$" shows two very different types of secondary particles. The first one is a set of

small aggregates (1-5 µm) and the second one consists of with aggregates from 10 to 200 µm (**Fig S9**). Further zooming of the aggregates reveals of what could be seen as primary particles of 30-100 nm. However, the size of these apparent primary particles does not agree with that determined by X-ray diffraction and the Scherrer equation. These nanometric particles could in fact be agglomerates of even smaller particles that cannot be distinguished by SEM. This could be due to the synthesis route: mechanosynthesis does not allow crystal growth. Li_2MnO_2F obtained "from Mn_2O_3" display particles of the same sizes as the other pathway. No regular geometry was observed for the aggregates or the particles. **Figure S9** shows the evolution of the aggregates through the different milling times with less zoomed areas as well as their evolution during the synthesis. Again, there is no clear difference between the morphology and size of the particles obtained by the two methods.

Electrochemical characterization:

Three cycles of cyclic voltammetry (CV) were performed on samples from the two different pathways for the different milling times (Figure 11). One main distinction can be established first between the two set of precursors. "From Mn_2O_3" pathway, none of the precursors were electrochemically active, while $LiMnO_2$ is in the other route[18,29]. The irreversible peak observed at 3.7 V for t=0h (**Fig. 11.b**) indicates thus an irreversible modification in the crystallographic structure of $LiMnO_2$ from orthorhombic to cubic, as it has been reported previously[18,30,31]. Therefore, the 6 h sample "from $LiMnO_2$" pathway exhibited more electrochemical activity compared to the 6 h sample "from Mn_2O_3". Furthermore, the CV for the 6 h sample obtained "from $LiMnO_2$" almost perfectly coincided with that of the 18 h and 36 h samples. However, the 6 h sample obtained "from Mn_2O_3" pathway showed hardly any Mn redox peaks.

For two final compounds, obtained after 36h of grinding, the Mn redox peaks appeared at 3.74 V versus Li^+/Li for Mn(III) oxidation and at 3.3 V for the Mn(IV) reduction. Thus a voltage difference of 0.44 V is observed between the cathodic and anodic peaks, that could come from the slow lithium diffusion kinetics in the percolating network. Indeed, the size of the aggregates could explain Li difficulty to percolate through the particles and justify the high overpotential between the charge and the discharge. This voltage hysteresis is a well-known issue for DRS material based on Mn redox[32–35].

A second redox activity could be noticed at higher potential, at 4.3 V in oxidation and 4.0 V in reduction. It is attributed to the O-redox mechanism and commonly observed for the first cycles with this kind of material[5,15,16]. The phenomenon is almost not reversible as it strongly decreases as soon as the 2nd cycle begins (**Fig 11a and 11b**). Therefore it is possible that the O-redox reactions might produce gaseous molecular O_2 species [15]. This is supported by other works which demonstrated that oxygen radicals ($O^{\bullet-}$) and peroxo-like (O_2^{n-}) are more easily reversible, in contrast what was observed in this work[36,37].

A third and last peak was of interest and occurs at 4.8 V, which indicated the electrolyte oxidation. Going above 4.6 V was proved necessary as tests displayed in **Figure S10** evidenced that 4.6 V was not a high enough potential to trigger O-redox mechanisms or to properly distinguish it from Mn redox. As a result, at 4.8 V the electrolyte reaches the end of its potential stability window and start being oxidized.

It was also worth highlighting that it took three cycles for the CV of both materials to be perfectly overlaid. Indeed, in the first two cycles, the O-redox peak at 4.45 V vs Li^+/Li in oxidation for "from $LiMnO_2$" pathway varied from 57 $mA \cdot g^{-1}$ to 40 $mA \cdot g^{-1}$ whereas for the "from Mn_2O_3" pathway the normalized intensity of the current at this point was weaker with 47 $mAh.g^{-1}$ moving

to 42 mAh.g^{-1}. It could be originated from different kinetics associated with O-redox but also slight variation in electrode thickness as self-supported PTFE electrode tends to be harder to work with.

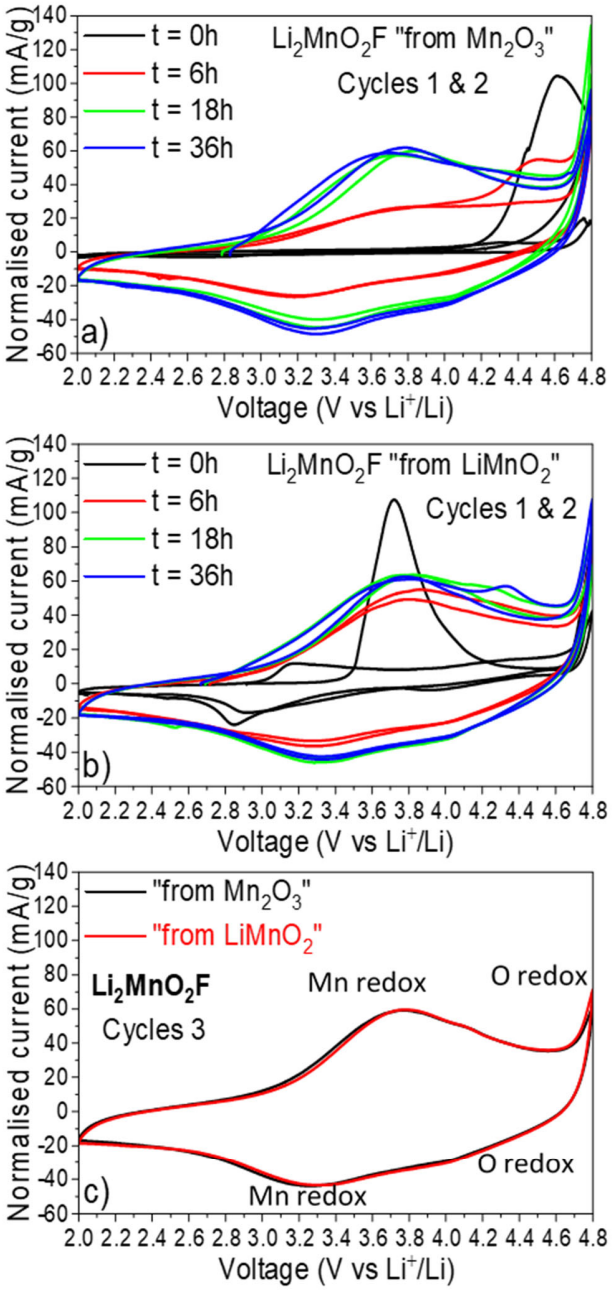

Figure 11. *Cyclic Voltammetry recorded for mixtures at different durations of ball milling for a) pathway "Mn_2O_3" b) pathway "$LiMnO_2$" and c) overlay of obtained Li_2MnO_2F, all cycled at 0.1mV/s in half cells vs metallic Li.*

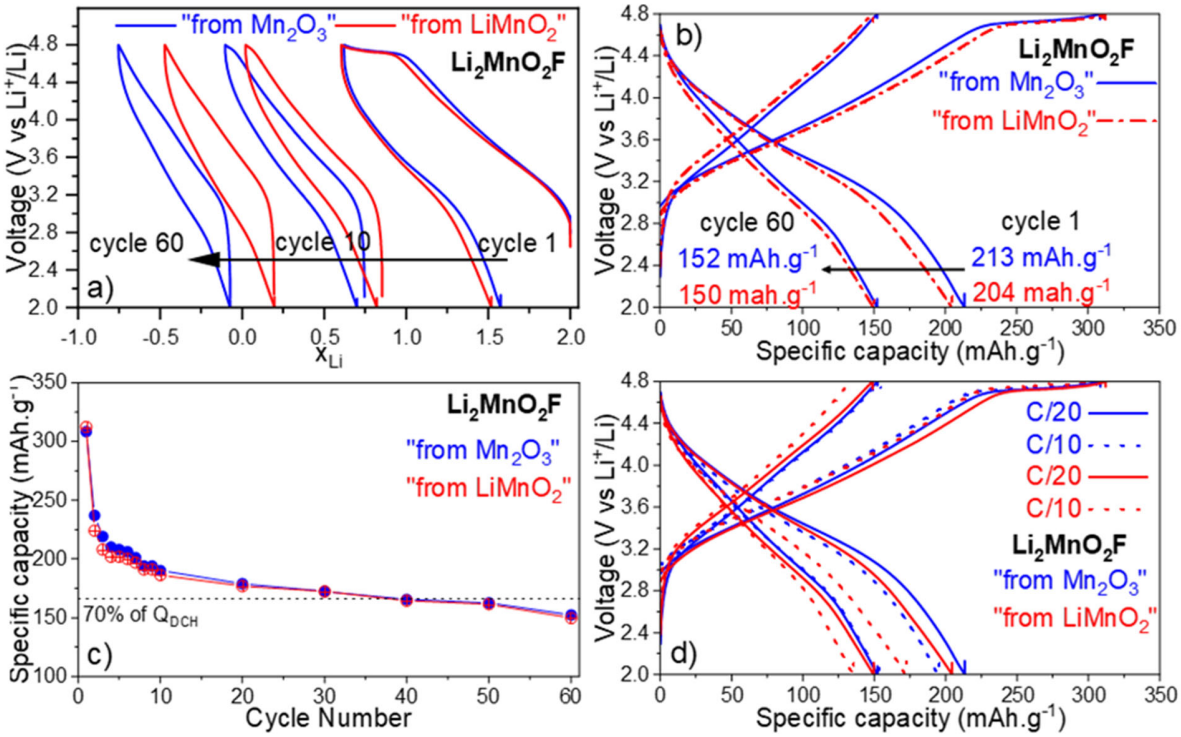

Figure 12. *a) Voltage profile as a function of x_{Li}, b) Comparison of Li_2MnO_2F from the two pathways by galvanostatic cycling at C/20 in half cells vs Li metal with E_{OCV} = 2.79 V and 2.65 V respectively for pathway "from Mn_2O_3" and "from $LiMnO_2$" c) Specific capacity and capacity retention evolution vs the 1st discharge during cycling with an emphasis on the 10 first cycles, d) C-rate comparison for C/10 & C/20.*

The galvanostatic cycling curves for Li_2MnO_2F obtained following the two different pathways are shown in **Figure 12,** with reproducibility and extensive galvanostatic cycling **Figure S11 and S12**. The cycling behavior capacities achieved after the first charge are very similar for the two samples (approximately 310 $mAh.g^{-1}$). As observed for the cyclic voltammetry, an irreversible mechanism associated with the voltage plateau at 4.75 V took place for the two samples above 4.6 V vs Li. It corresponds to a deintercalation of more than one mole of Li per formula unit where Mn(III) oxidation had already been completed with the full oxidation to Mn(IV) if only the manganese oxidation is considered (**Fig. 12.a**). This plateau has not been observed in first cycle

voltage profile reported earlier in the literature[3,38] and may result from electrolyte decomposition at high voltage, reinforced by the continuous shift of lithium content towards low values at the end of charge (**Fig. 12.a**). However, the high voltage plateau at 4.75 V in charge could also correspond to oxygen oxidation and oxygen loss due to the irreversible oxygen oxidation at the first charge cannot be totally excluded either. At this stage, further investigation would be required to distinguish which phenomenon is predominant.

Figure 12.c exhibits that the two materials are very similar from the first to the 60th cycles with very little difference between the capacities. Capacities for both pathways decreased to 150 mAh.g^{-1} after 60 cycles. However, the capacity retention remained above 70% of the first discharge capacity after 60 cycles which, compared to literature, corresponded to usual performances for this material[5]. This shows that Li_2MnO_2F exhibits nearly identical performances regardless of the pathway and is likely to not be impacted by the precursors.

C/20 is a slow cycling rate, allowing enough time for Li to percolate through the lattice, therefore the same study was conducted at a cycling rate twice as fast: C/10 displayed **Figure 12.d**. For the first charge, Li_2MnO_2F "from Mn_2O_3" exhibited a specific capacity of 305 mAh.g^{-1}, which was similar to that obtained at C/20: 304 mAh.g^{-1}, whereas for Li_2MnO_2F "from $LiMnO_2$" the capacity was slightly lower at 297 mAh.g^{-1} compared to 319 mAh.g^{-1} at C/20. The capacity loss was also more significant after the first discharge at C/10 rate. These losses are associated with the Li intercalation kinetics. At C/20 the lithium ions have of slightly more time to percolate through the bulk, however no major differences were noticed between the two C-rates. Over cycling, these losses tend to reduce, at the 60th cycle, the $\Delta C_{\frac{c}{20}-\frac{c}{10}}$ was almost null for Li_2MnO_2F "from Mn_2O_3" pathway and decreased to approximately 15 mAh.g^{-1} for Li_2MnO_2F "from $LiMnO_2$". For the first cycles, the difference lied in the slower kinetics of the O-redox, and after 60 cycles the O-redox

was exhausted and the electrochemical reaction relied only on the Mn(III)/Mn(IV) couple, explaining the little difference observed.

Conclusion:

This study has shown that regardless of the choice of precursors, either Mn_2O_3 or $LiMnO_2$ the occupation of the cationic sub lattice sites is not fully random. The diamagnetic environments, favorable to Li percolation network represent about 6 % of Li environments. This study also evidenced the necessity of the extended mechanosynthesis duration as the reaction continued to occur at the short range scale. The small variation in the precursor choice has no impact on Li_2MnO_2F synthesized by mechanosynthesis and could be synthesized through two distinct pathways without any performance threatening differences. X-ray diffraction shows that the average structure is the same for both Li_2MnO_2F compounds obtained through different pathways. ^{7}Li and ^{19}F NMR both displays a good overlaying of the spectra indicating that the local structure is also similar in the two samples. Moreover, both Li_2MnO_2F were able to deliver an average specific capacity of more than 200 $mAh.g^{-1}$ after the first discharge. It retains over 70% of its capacity (150 $mAh.g^{-1}$) over 60 cycles at C/10 and C/20 C-rates. Finally, no strong difference was observed between the two Li_2MnO_2F, either from a structural, nor from an electrochemical point of view. Therefore, it is possible to conclude that for the mechanosynthesis of Li_2MnO_2F the chosen set of precursors have little impact compared to other conditions such as the amount of beads or the duration of the mechanosynthesis.

Supporting Information

Additional information regarding the experimental conditions (synthesis, NMR), additional NMR spectra and information concerning the spectra decomposition and analysis, XRD pattern of the Mn_2O_3 precursor used, SEM images and additional cycling curves (PDF)

Acknowledgements :

The authors would like to thank the Région Nouvelle Aquitaine and SAFT Company for their financial support (Project ROSALIE – APPR2020-2019-8290710).

XAS measurements were supported by CERIC in the frame of proposal 20207080. Lorenzo Stievano is greatly acknowledged for sharing the beamtime. We thank Giuliana Aquilanti and Gangadhar Das for their help during the XAS experiments, Mathieu Duttine for help with the NMR spectrometers and Sonia Buffiere for SEM imaging.

Bibliography:

(1) Chen, D.; Ahn, J.; Chen, G. An Overview of Cation-Disordered Lithium-Excess Rocksalt Cathodes. *ACS Energy Lett.* **2021**, 1358–1376. https://doi.org/10.1021/acsenergylett.1c00203.
(2) Lee, J.; Urban, A.; Li, X.; Su, D.; Hautier, G.; Ceder, G. Unlocking the Potential of Cation-Disordered Oxides for Rechargeable Lithium Batteries. *Science* **2014**, *343* (6170), 519–522. https://doi.org/10.1126/science.1246432.
(3) Clément, R. J.; Lun, Z.; Ceder, G. Cation-Disordered Rocksalt Transition Metal Oxides and Oxyfluorides for High Energy Lithium-Ion Cathodes. *Energy Environ. Sci.* **2020**, *13* (2), 345–373. https://doi.org/10.1039/C9EE02803J.
(4) Lee, J.; Seo, D.-H.; Balasubramanian, M.; Twu, N.; Li, X.; Ceder, G. A New Class of High Capacity Cation-Disordered Oxides for Rechargeable Lithium Batteries: Li–Ni–Ti–Mo Oxides. *Energy Environ. Sci.* **2015**, *8* (11), 3255–3265. https://doi.org/10.1039/C5EE02329G.

(5) House, R. A.; Jin, L.; Maitra, U.; Tsuruta, K.; Somerville, J. W.; Förstermann, D. P.; Massel, F.; Duda, L.; Roberts, M. R.; Bruce, P. G. Lithium Manganese Oxyfluoride as a New Cathode Material Exhibiting Oxygen Redox. *Energy Environ. Sci.* **2018**, *11* (4), 926–932. https://doi.org/10.1039/C7EE03195E.
(6) Chen, R.; Ren, S.; Knapp, M.; Wang, D.; Witter, R.; Fichtner, M.; Hahn, H. Disordered Lithium-Rich Oxyfluoride as a Stable Host for Enhanced Li $^{+}$ Intercalation Storage. *Adv. Energy Mater.* **2015**, *5* (9), 1401814. https://doi.org/10.1002/aenm.201401814.
(7) Ateba Mba, J.-M.; Arčon, I.; Mali, G.; Tchernychova, E.; Witte, R.; Kruk, R.; Gaberšček, M.; Dominko, R. Ceramic Synthesis of Disordered Lithium Rich Oxyfluoride Materials. *J. Power Sources* **2020**, *467*, 228230. https://doi.org/10.1016/j.jpowsour.2020.228230.
(8) Wang, R.; Li, X.; Liu, L.; Lee, J.; Seo, D.-H.; Bo, S.-H.; Urban, A.; Ceder, G. A Disordered Rock-Salt Li-Excess Cathode Material with High Capacity and Substantial Oxygen Redox Activity: Li 1.25 Nb 0.25 Mn 0.5 O 2. *Electrochem. Commun.* **2015**, *60*, 70–73. https://doi.org/10.1016/j.elecom.2015.08.003.
(9) Yabuuchi, N.; Nakayama, M.; Takeuchi, M.; Komaba, S.; Hashimoto, Y.; Mukai, T.; Shiiba, H.; Sato, K.; Kobayashi, Y.; Nakao, A.; Yonemura, M.; Yamanaka, K.; Mitsuhara, K.; Ohta, T. Origin of Stabilization and Destabilization in Solid-State Redox Reaction of Oxide Ions for Lithium-Ion Batteries. *Nat. Commun.* **2016**, *7* (1), 13814. https://doi.org/10.1038/ncomms13814.
(10) Freire, M.; Kosova, N. V.; Jordy, C.; Chateigner, D.; Lebedev, O. I.; Maignan, A.; Pralong, V. A New Active Li–Mn–O Compound for High Energy Density Li-Ion Batteries. *Nat. Mater.* **2016**, *15* (2), 173–177. https://doi.org/10.1038/nmat4479.
(11) Takeda, N.; Hoshino, S.; Xie, L.; Chen, S.; Ikeuchi, I.; Natsui, R.; Nakura, K.; Yabuuchi, N. Reversible Li Storage for Nanosize Cation/Anion-Disordered Rocksalt-Type Oxyfluorides: LiMoO 2 – x LiF ($0 \leq x \leq 2$) Binary System. *J. Power Sources* **2017**, *367*, 122–129. https://doi.org/10.1016/j.jpowsour.2017.09.060.
(12) Ji, H.; Urban, A.; Kitchaev, D. A.; Kwon, D.-H.; Artrith, N.; Ophus, C.; Huang, W.; Cai, Z.; Shi, T.; Kim, J. C.; Kim, H.; Ceder, G. Hidden Structural and Chemical Order Controls Lithium Transport in Cation-Disordered Oxides for Rechargeable Batteries. *Nat. Commun.* **2019**, *10* (1), 592. https://doi.org/10.1038/s41467-019-08490-w.
(13) Kan, W. H.; Deng, B.; Xu, Y.; Shukla, A. K.; Bo, T.; Zhang, S.; Liu, J.; Pianetta, P.; Wang, B.-T.; Liu, Y.; Chen, G. Understanding the Effect of Local Short-Range Ordering on Lithium Diffusion in Li1.3Nb0.3Mn0.4O2 Single-Crystal Cathode. *Chem* **2018**, *4* (9), 2108–2123. https://doi.org/10.1016/j.chempr.2018.05.008.
(14) Diaz-Lopez, M.; Freire, M.; Joly, Y.; Colin, C. V.; Fischer, H. E.; Blanc, N.; Boudet, N.; Pralong, V.; Bordet, P. Local Structure and Lithium Diffusion Pathways in Li $_4$ Mn $_2$ O $_5$ High Capacity Cathode Probed by Total Scattering and XANES. *Chem. Mater.* **2018**, *30* (9), 3060–3070. https://doi.org/10.1021/acs.chemmater.8b00827.
(15) Sharpe, R.; House, R. A.; Clarke, M. J.; Förstermann, D.; Marie, J.-J.; Cibin, G.; Zhou, K.-J.; Playford, H. Y.; Bruce, P. G.; Islam, M. S. Redox Chemistry and the Role of Trapped Molecular O $_2$ in Li-Rich Disordered Rocksalt Oxyfluoride Cathodes. *J. Am. Chem. Soc.* **2020**, *142* (52), 21799–21809. https://doi.org/10.1021/jacs.0c10270.
(16) McColl, K.; House, R. A.; Rees, G. J.; Squires, A. G.; Coles, S. W.; Bruce, P. G.; Morgan, B. J.; Islam, M. S. Transition Metal Migration and O2 Formation Underpin Voltage Hysteresis in Oxygen-Redox Disordered Rocksalt Cathodes. *Nat. Commun.* **2022**, *13* (1), 5275. https://doi.org/10.1038/s41467-022-32983-w.

(17) Guegan, D. Stabilisation de matériaux d'électrode positive pour batteries Li-ion de structure désordonnée type NaCl: synthèse et caractérisation. 175.
(18) Croguennec, L.; Deniard, P.; Brec, R.; Lecerf, A. Preparation, Physical and Structural Characterization of LiMnO2 Samples with Variable Cationic Disorder. *J. Mater. Chem.* **1995**, *5* (11), 1919. https://doi.org/10.1039/jm9950501919.
(19) Dusek, M.; Petricek, V. Towards the Routine Application of Computing System Jana2000. *Acta Crystallogr. A* **2005**, *61* (a1), c104–c105. https://doi.org/10.1107/S0108767305095565.
(20) Momma, K.; Izumi, F. *VESTA 3* for Three-Dimensional Visualization of Crystal, Volumetric and Morphology Data. *J. Appl. Crystallogr.* **2011**, *44* (6), 1272–1276. https://doi.org/10.1107/S0021889811038970.
(21) Journal of Synchrotron Radiation - 2005 - Ravel - ATHENA ARTEMIS HEPHAESTUS Data Analysis for X-ray Absorption.Pdf.
(22) Shannon, R. D.; Prewitt, C. T. Revised Values of Effective Ionic Radii. *Acta Crystallogr. B* **1970**, *26* (7), 1046–1048. https://doi.org/10.1107/S0567740870003576.
(23) Clément, R. J.; Kitchaev, D.; Lee, J.; Gerbrand Ceder. Short-Range Order and Unusual Modes of Nickel Redox in a Fluorine-Substituted Disordered Rocksalt Oxide Lithium-Ion Cathode. *Chem. Mater.* **2018**, *30* (19), 6945–6956. https://doi.org/10.1021/acs.chemmater.8b03794.
(24) Clément, R. J.; Lun, Z.; Ceder, G. Cation-Disordered Rocksalt Transition Metal Oxides and Oxyfluorides for High Energy Lithium-Ion Cathodes. *Energy Environ. Sci.* **2020**, *13* (2), 345–373. https://doi.org/10.1039/C9EE02803J.
(25) Geng, F.; Hu, B.; Li, C.; Zhao, C.; Lafon, O.; Trébosc, J.; Amoureux, J.-P.; Shen, M.; Hu, B. Anionic Redox Reactions and Structural Degradation in a Cation-Disordered Rock-Salt Li $_{1.2}$ Ti $_{0.4}$ Mn $_{0.4}$ O $_{2}$ Cathode Material Revealed by Solid-State NMR and EPR. *J. Mater. Chem. A* **2020**, *8* (32), 16515–16526. https://doi.org/10.1039/D0TA03358H.
(26) Carlier, D.; Ménétrier, M.; Grey, C. P.; Delmas, C.; Ceder, G. Understanding the NMR Shifts in Paramagnetic Transition Metal Oxides Using Density Functional Theory Calculations. *Phys. Rev. B* **2003**, *67* (17), 174103. https://doi.org/10.1103/PhysRevB.67.174103.
(27) Grey, C. P.; Lee, Y. J. Lithium MAS NMR Studies of Cathode Materials for Lithium-Ion Batteries. *Solid State Sci.* **2003**, *5* (6), 883–894. https://doi.org/10.1016/S1293-2558(03)00113-4.
(28) Lun, Z.; Ouyang, B.; Cai, Z.; Clément, R. J.; Kwon, D.-H.; Huang, J.; Papp, J. K.; Balasubramanian, M.; Tian, Y.; McCloskey, B. D.; Ji, H.; Kim, H.; Kitchaev, D. A.; Ceder, G. Design Principles for High-Capacity Mn-Based Cation-Disordered Rocksalt Cathodes. *Chem* **2020**, *6* (1), 153–168. https://doi.org/10.1016/j.chempr.2019.10.001.
(29) Croguennec, L. INFLUENCE DE LA MORPHOLOGIE ET DES DEFAUTS D'EMPILEMENT SUR LE COMPORTEMENT ELECTROCHIMIQUE DU SYSTEME $LiMnO_2$ ORTHORHOMBIQUE, Université de Nantes, Nantes, France, 1996.
(30) Croguennec, L. Electrochemical Behavior of Orthorhombic LiMnO2: Influence of the Grain Size and Cationic Disorder. *Solid State Ion.* **1996**, *89* (1–2), 127–137. https://doi.org/10.1016/0167-2738(95)00245-6.
(31) Croguennec, L.; Deniard, P.; Brec, R. Electrochemical Cyclability of Orthorhombic LiMnO2 : Characterization of Cycled Materials. *J. Electrochem. Soc.* **1997**, *144* (10), 3323–3330. https://doi.org/10.1149/1.1838013.
(32) Li, B.; Sougrati, M. T.; Rousse, G.; Morozov, A. V.; Dedryvère, R.; Iadecola, A.; Senyshyn, A.; Zhang, L.; Abakumov, A. M.; Doublet, M.-L.; Tarascon, J.-M. Correlating Ligand-to-

Metal Charge Transfer with Voltage Hysteresis in a Li-Rich Rock-Salt Compound Exhibiting Anionic Redox. *Nat. Chem.* **2021**, *13* (11), 1070–1080. https://doi.org/10.1038/s41557-021-00775-2.

(33) Wu, Z.; Cheng, Y.; Shi, Y.; Xia, M.; Zhang, Y.; Hu, X.; Zhou, X.; Chen, Y.; Sun, J.; Liu, Y. Restriction of Voltage Decay by Limiting Low-Voltage Reduction in Li-Rich Oxide Materials. *J. Colloid Interface Sci.* **2022**, *620*, 57–66. https://doi.org/10.1016/j.jcis.2022.03.101.

(34) Abulikemu, A.; Matsunaga, T.; Watanabe, A.; Yamamoto, K.; Uchiyama, T.; Nakanishi, K.; Kawaguchi, S.; Osaka, K.; Uchimoto, Y. Rocksalt Type Li2Nb0·15Mn0·85O3 without Structure Degradation or Redox Evolution upon Cycling. *J. Alloys Compd.* **2021**, *853*, 156984. https://doi.org/10.1016/j.jallcom.2020.156984.

(35) Yue, Y.; Li, N.; Li, L.; Foley, E. E.; Fu, Y.; Battaglia, V. S.; Clément, R. J.; Wang, C.; Tong, W. Redox Behaviors in a Li-Excess Cation-Disordered Mn–Nb–O–F Rocksalt Cathode. *Chem. Mater.* **2020**, *32* (11), 4490–4498. https://doi.org/10.1021/acs.chemmater.9b05221.

(36) Grenier, A.; Kamm, G. E.; Li, Y.; Chung, H.; Meng, Y. S.; Chapman, K. W. Nanostructure Transformation as a Signature of Oxygen Redox in Li-Rich 3d and 4d Cathodes. *J. Am. Chem. Soc.* **2021**, *143* (15), 5763–5770. https://doi.org/10.1021/jacs.1c00497.

(37) Li, Q.; Ning, D.; Zhou, D.; An, K.; Wong, D.; Zhang, L.; Chen, Z.; Schuck, G.; Schulz, C.; Xu, Z.; Schumacher, G.; Liu, X. The Effect of Oxygen Vacancy and Spinel Phase Integration on Both Anionic and Cationic Redox in Li-Rich Cathode Materials. *J. Mater. Chem. A* **2020**, *8* (16), 7733–7745. https://doi.org/10.1039/D0TA02517H.

For Table of Contents Only

Mechanosynthesis of disordered rocksalt Li_2MnO_2F used as positive electrode materials in lithium-ion batteries, from to sets of precursors. The monitoring of the reaction progress has been done by ^{7}Li and ^{19}F MAS-NMR to understand the evolution of the local environments as well as the formation of the disordered rocksalt phase. This allowed to identify an optimal milling time to reach the final compounds. The electrochemical properties of the compounds are also reported.